

Article

The Utilization of Carbon Dioxide to Prepare TiC_xO_y Films with Low Friction and High Anti-Corrosion Properties

Kaixiong Gao ^{1,2,†}, Zhaolong Wang ^{1,†}, Qian Jia ^{1,2}, Bin Zhang ^{1,*}, Zhixing Mou ^{1,3} and Junyan Zhang ^{1,2,*}

¹ Key Laboratory of Science and Technology on Wear and Protection of Materials, Lanzhou Institute of Chemical Physics, Chinese Academy of Sciences, Lanzhou 730000, China; kxgao@licp.cas.cn (K.G.); wangzldyx@163.com (Z.W.); jiaqian1@licp.cas.cn (Q.J.); 18693187088@163.com (Z.M.)

² Center of Materials Science and Optoelectronics Engineering, University of Chinese Academy of Sciences, Beijing 100049, China

³ College of Petrochemical Technology, Lanzhou University of Technology, Lanzhou 730050, China

* Correspondence: bzhang@licp.cas.cn (B.Z.); zhangjunyan@licp.cas.cn (J.Z.); Tel.: +86-9314968199 (B.Z.); +86-9314968295 (J.Z.)

† These authors contributed equally to this work.

Received: 1 May 2020; Accepted: 28 May 2020; Published: 30 May 2020



Abstract: Recycling carbon dioxide (CO_2) for weakening the greenhouse effect is still an outstanding question. Although many chemical methods have been designed for CO_2 conversion, they is still a need to develop new ways for CO_2 recycling. Plasma methods were employed to convert CO_2 into energy molecules, with the addition of H_2 , H_2O and so on. Non heavy elements, like Ti, Cr, Si and Mo and so forth, were employed to take part in a reactive process, which might be very interesting for special scientific interest. In this work, magnetron sputtering method was used not only for igniting the plasma but also for providing Ti elements involved in reactions, via the selected Ti target. One can confirm that the TiC_xO_y films were successfully grew via sputtering a Ti target in CO_2 atmosphere with Ar as dilute gas, which proved that CO_2 is a key player in the matter of the involvement of excited CO_2^+ , CO^+ , CO_3^- and so on, in the growth process reacting with Ti ions. The TiC_xO_y films exhibit the highest hardness (20.3 GPa), lowest friction coefficient (0.065) and the best corrosion resistance. The growth of the TiC_xO_y films are not only a new strategy for consuming CO_2 but also a good way for reusing it for preparing TiC_xO_y films with high hardness for anti-corrosion and reducing friction. Moreover, reducing CO_2 emissions via energy saving (through reducing friction and corrosion resistance) and recycling existing CO_2 are both important for mitigating the greenhouse effect.

Keywords: carbon dioxide; CO_2 conversion; high hardness; low friction; corrosion resistance; TiC_xO_y films

1. Introduction

In the atmosphere, carbon dioxide (CO_2) acts rather like a one-way mirror in the roof of a greenhouse, which allows sunlight to enter but prevents heat from escaping. CO_2 is emitted in a number of ways such as burning of oil, coal, gas, petrol and deforestation and so forth [1,2]. The more CO_2 accumulates, the higher temperatures rise. To solve global warming problems and to recycle CO_2 as a resource, there is a crying need for methods to capture, storage and recycle of CO_2 [3–6]. At present, there are lots of methods for carbon dioxide capturing and conversion, such as electrocatalytic reduction by heterogeneous materials, photocatalytic conversion of CO_2 to CH_4 [6], hydrogen reduction by

efficient catalysts of CO₂ to methanol [7], utilization of CO₂ as lubricants, and the storage of CO₂ in subsurface reservoirs [8,9].

Using CO₂ as a resource for the creation of new raw materials has been extensively studied. Ali Reza Kamali designed an innovative approach that used a reactive LiCl-Li₂O molten salt method (the injection of moist CO₂ into molten LiCl containing Li₂O), of which diamond crystallites within lithium carbonate were obtained with an average nanocrystallite size of about 44 nm [10]. Feng Shi et al. created a synthetic nano- and molecular catalytic material via catalytic synthesis of nitrogen doped carbon layers on AlO_x supported nano-Cu, which can finely tune the catalytic performance of the supported copper catalyst that is generated in situ by the reaction of CuAlO_x and 1,10-Phen in the presence of hydrogen. Thanks to the nano- and molecular synergistic effect, the synthetic catalytic material could be used for the controllable synthesis of *N,N*-dimethylformamide (DMF) from dimethylamine and CO₂/H₂ by blocking the reaction pathways of further catalytic hydrogenation of DMF to N(CH₃)₃ [11]. Further, the Pt-modified TiO₂ (Pt/TiO₂) is the most systematic investigated system for photocatalytic CO₂ conversion. Via an easy electron-spinning method, Zhang et al. grew Au and Pt NP coloaded TiO₂ nanofibers (NFs). Compared to pure TiO₂, Au-loaded TiO₂ and Pt-loaded TiO₂, respectively [12]. This new catalyst system showed a higher activity for CO₂ reduction with H₂O vapor to CH₄, which can be ascribed to the synergistic effect of both electron-extracting capacity of Pt NPs as a cocatalyst and surface plasmon resonance of Au NPs [12]. Kalantar-Zadeh et al. exploited the formation of a cerium oxide catalyst at the liquid metal/electrolyte interface, combined with cerium nanoparticles, which can promote the room temperature reduction of CO₂. They discovered that at a low onset potential of −310 mV vs CO₂/C, layered solid carbonaceous species were synthesized. These new obtained solid carbonaceous materials could be utilized for the fabrication of high-performance capacitor electrodes [13]. Hyunwoong Park et al. reported CuFeO₂ and CuO mixed p-type catalysts, which was grown via widely employed electroplating of earth abundant cupric and ferric ions and followed by annealing under open atmospheric air. They confirmed that RHE in CO₂-purged bicarbonate solution and converted CO₂ to formate with over 90% selectivity under simulated solar light (air mass 1.5, 100 mW·cm^{−2}) [14]. Besides the catalyst method, there are continuous attempts to find another way of converting CO₂ into micromolecule organics.

More recently, another novel strategy, plasma technology, has attracted more consideration from scientists. Guoxing Chen et al. developed a surface-wave microwave discharge method and evaluated the CO/H₂ ratio and the specific energy input (SEI) on the influence of products. They believed that syngas with a ratio close to 1 can be produced when the CO₂-H₂O ratio in the gas mixture is 50:50, while the optimum SEI for this gas mixture ratio is 1.6 eV/mol [15]. Han S. Uhm et al. employed 2.45 GHz microwave inspired plasma torch under atmospheric pressure to splitting CO₂ and the carbon monoxide molecules, carbon atoms and oxygen atoms were confirmed by optical spectroscopy. They thought that, at a high-temperature, the CO₂ torch has the potential to be applied to hydrocarbon fuel reforming at one atmospheric pressure [16]. During the plasma process, CO₂ always recombine into CO₂⁺, CO⁺, CO₃[−], CO₄[−], CO₄⁺, C₂O₄⁺, C₂O₃⁺, C₂O₂ and other related materials, then the introduction of N₂, H₂ and H₂O will introduce newborn charged functional groups, which highly depend on the incoming gases in the reaction system [17]. One should notice that all the mentioned plasma conversion processes are related to gas resource, a solid material was not employed, which is probably because a gas resource, like N₂, H₂ and H₂O, benefit the synthesis of energy molecules or related chemical intermediates. However, no energy molecule is fond of atoms that compose solid elements in nature. Fascinatingly, one can guess what will happen if we bring solid elements into a plasma reactive process, like Ti, Cr, Si, Mo and so forth.

It is worth noting that reactive magnetron sputtering technology is a useful way to grow low friction solid films, such as TiN_x, CrN_x, TiC_x and CrC_x films and diamond-like carbon films as well as fullerene-like hydrogen carbon films [18–26], which show not only low friction or even superlubricity but also high anti-corrosive properties via magnetron sputtering method [27–31]. Further, the so-called metallic oxycarbides MeO_xC_y, produced by magnetron sputtering, have attracted the interest of

materials scientists. A virtual certainty is that the introduction of oxygen allows the tailoring of “pure” metal carbides such as the band-gap, bandwidth, electronic and mechanic and friction properties [32–34]. Bringing oxygen into metal carbides films has a strong influence on the films’ structure. A.C. Fernandes et al. studied the influence of the O/C ratio on the structure of TiC_xO_y films and they drew a phase diagram which can be divided into 3 different regimes. A carbide zone (I), a transition zone (II) and an oxide (III), corresponding to the crystal structure of TiC, poorly crystallized fcc TiC and TiO phases mixed into an amorphous matrix and an amorphous structure, respectively [32,33]. As a matter of fact, most of the work on MeO_xC_y films are connected to optic and electronic properties, while very few are related to mechanic and friction properties [32–34]. M.T. Mathew et al. investigated the friction, corrosion and tribocorrosion properties of TiC_xO_y films, both in artificial sweat solutions and bio-fluids [35,36]. Their results showed that the corrosion behavior of TiC_xO_y films is more correlated to bulk inner-structure of the films [35,36]. However, those referred TiC_xO_y films are all obtained via magnetron sputtering in an oxide atmosphere, using the carbon target as a carbon source and the tribology of TiC_xO_y films in moist air or pure water has not been reported before.

As we know, employing CO_2 as a feeding gas to grow oxycarbide films not only solidifies CO_2 but also reduces CO_2 via energy saving from reducing friction. In consideration of the above properties, the CO_2 is selected as feed gas to deposit TiC_xO_y films at the first time in present work. A series of films with different components were prepared on silicon wafers by changing the sputtering current of Ti target. The composition and structure of the as-obtained films were analyzed by scanning electron microscope (SEM), X-ray photoelectron spectroscopy (XPS) and X-ray diffraction (XRD). The mechanical, frictional and anticorrosive properties were also investigated by Nano Indenter, Tribometer and electrochemical workstation, respectively. Furthermore, the reasons for the high hardness, low friction and good corrosion resistance of the as-obtained TiC_xO_y films are proposed based on the structure and property characterization results. This work points out a new strategy for the conversion and utilization of CO_2 via growth films for anti-wear and anti-corrosion purpose.

2. Materials and Methods

2.1. Films Preparation

The films were deposited on Si wafers (100) by a magnetron sputtering system. Titanium was used as the sputtering target. The gas of CO_2 was used as a feed gas. The possible reactions pathway that favor CO_2 conversion, using Ar as a dilution gas, are shown in Equations (1)–(3) [37].



Thus, these charged ions will react with metal, like Ti, to grow TiC_xO_y films possibly.

Prior to depositing the films, the substrates (Si wafers) were ultrasonically cleaned in ethanol for about 30 min and were rapidly transferred into the vacuum chamber. Then the oxidation layer of Si substrates was removed by Ar^+ (the negative bias of 900 V, pulsed frequency of 60 kHz and duty cycle of 0.6). The detailed deposition parameters for the TiC_xO_y films are presented in Table 1 and the samples are marked as T1-T5 corresponding to the settled current, respectively.

Table 1. The deposition parameters for the TiC_xO_y films.

Films	Ar (sccm)	CO ₂ (sccm)	Negative bias (V)	Target Current (A)	Deposited Times (h)
T1	50	10	150	0.65	1
T2	50	10	150	0.80	1
T3	50	10	150	0.95	1
T4	50	10	150	1.1	1
T5	50	10	150	1.25	1

2.2. Characterization Methods

The Nano-indenter DCM system, XRD (Bruker D8Discover25, AXS, Karlsruhe, Germany), XPS (Al-Ka radiation), SEM (JSM-6701F, JEOL, Tokyo, Japan) equipped with Energy dispersive spectrometer (EDS, JSM-5601LV, JEOL), electrochemical workstation (μ -AutolabIII, Metrohm, Herisau, Switzerland) were employed to characterize the composition, structure and properties of the as-obtained films. During the electrochemical tests, Ag/AgCl and Pt were respectively used as reference and counter electrodes. The electrochemical tests were performed in a 3.5 wt.% NaCl solution at room temperature and the tested area was 0.196 cm².

2.3. Friction Test

The reciprocally ball-on-disc tribometer (MFT-R4000) was employed to measure the friction properties of the films. The ceramic balls (Al₂O₃, Φ 5 mm) were used as the friction couples. The friction process was tested in a 3.5 wt.% NaCl water solution environment (the load of 10 N, sliding stroke of 5 mm and frequency of 10 Hz).

3. Results

3.1. The Mechanical and Frictional Performance of the Films

In order to investigate the mechanical performance of the TiC_xO_y films, the Nano-indenter DCM system was employed to analyze the hardness (H) and elastic modulus (E). Figure 1a illustrates the variation of the H and E for the TiC_xO_y films deposited at different target currents. From T1 to T5, the harnesses of TiC_xO_y films are 13.0 (T1), 17.3 (T2), 20.3 (T3), 19.4 (T4) and 16.3 (T5) GPa, respectively. Noticeably, a point of E inflexion turns out at target current of 0.80 A (T2) and shows a little change beyond the current of 0.80 A. It can be determined that the film owns the highest mechanical performance when the target current is 0.95 A (T3). Moreover, the values of H^3/E^2 for the TiC_xO_y films prepared at different target currents exhibit a similar change trend with hardness. These results elucidate that T3 probably has the most prominent friction properties [38,39].

To acknowledge this speculation, the friction coefficients were assured *via* a ball-on-disc tribometer in a 3.5 wt.% NaCl water solution. Figure 1(b) shows the average friction coefficients (μ) of the TiC_xO_y films deposited at different target currents. When the target currents change from 0.65 to 1.25 A, the average friction coefficients of the TiC_xO_y films are 0.091, 0.085, 0.065, 0.071 and 0.080, corresponding to T1, T2, T3, T4 and T5, respectively. The friction coefficients, likewise, show an extreme low value at the target current of 0.95 A (T3). The friction variation is contrary to the shift tendencies of hardness and H^3/E^2 . This result implies that T3 has great mechanical performance and a low coefficient of friction (Figure 1).

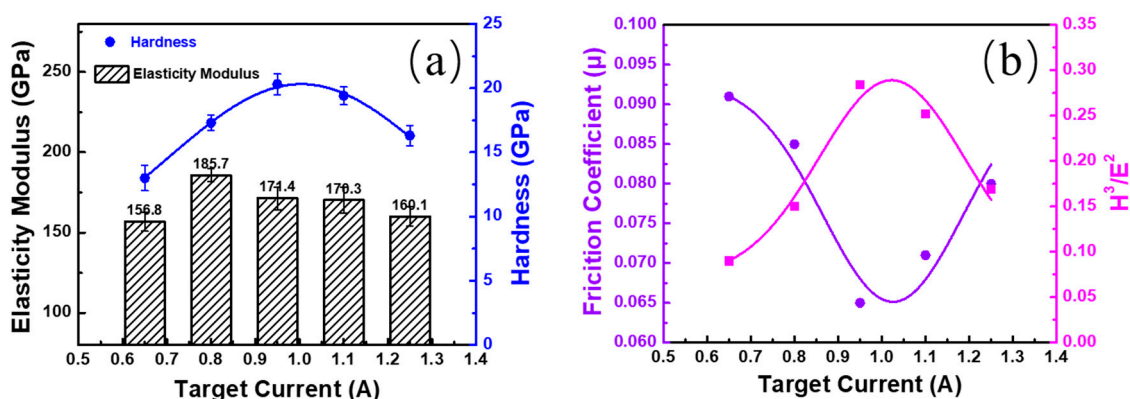


Figure 1. (a) The variation of hardness (H) and elastic modulus (E) for TiC_xO_y films deposited at different target current, (b) the change of friction coefficients and H^3/E^2 for the TiC_xO_y films deposited at different target current.

3.2. The Electrochemical Corrosion Performances of Films

The open circuit potential and polarization curve tests were carried out to evaluate the corrosion resistance of the obtained samples on the electrochemical workstation. Figure 2a,b shows the polarization curves of the TiC_xO_y films deposited at different sputter current in 3.5 wt.% NaCl solution. Obviously, the lowest corrosion current density of $0.024 \mu A/cm^2$ can be obtained for T3. Noticeably, with the sputter, currents increase from 0.65 to 0.80 A and the corrosion current density decreases three orders of magnitude ($1.83-0.033 \mu A/cm^2$). However, when the sputter current beyond 0.95 A, the corrosion current density increases along with the increase of sputter current, which are $0.34 \mu A/cm^2$ at 1.10 A and $257.42 \mu A/cm^2$ at 1.25 A, respectively, indicating that the corrosion resistance becomes worse. The corrosion current density of T5 (1.25 A) increases by five orders of magnitude compared with those of T3 (0.95A) and T2 (0.80 A).

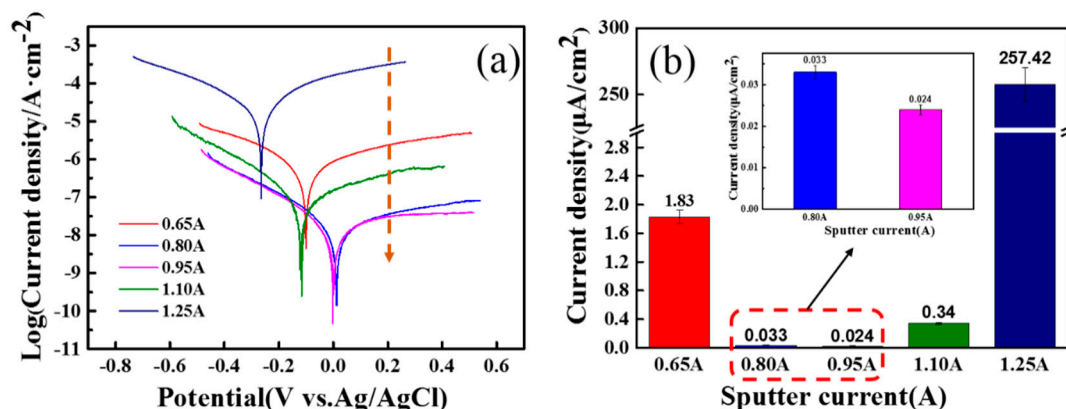


Figure 2. (a) Potentiodynamic polarization of TiC_xO_y films deposited at different sputter current in 3.5% NaCl solution; (b) Corrosion current density of TiC_xO_y films deposited at different sputter current at 0.2 V (vs. Ag/AgCl).

3.3. The XRD Results of Films

Figure 3a shows the XRD spectra of the TiC_xO_y films deposited at different target currents, revealing that strong diffraction peaks at about 37° , 43° and 62° are obtained for all the samples. These values are located between those of TiC (PDF No.: 32-1383) and $TiO_{1.04}$ (PDF No.: 43-1296) XRD patterns, which have strong diffraction peaks at 36.4° (111), 42.3° (200), 62.5° (220) and 37.3° (111), 43.3° (200), 63° (220) [40,41], respectively. Therefore, it can be speculated that C and O atoms are possibly replaced with each other which induced the lattice distortion, where the peak position drifts slightly

out of its original position, like silver-doping induced lattice distortion in TiO₂ nanoparticles [42]. More interestingly, when the target current was 0.8 A, the XRD pattern of TiC_xO_y films shows two peaks at about 52° (201) and 56° (221), which can be attributed to the standard XRD pattern of hexagonal corundum-type Ti₂O₃ (PDF, No. 43-1033) [43]. It should be noticed that the ratio of these two peaks varied with the increase of the target current. The peak at 52° (201) becomes gradually weak and the peak at 56° (221) disappeared while the target current increased, which is probably to be influenced by C/O substituting effects. It can be speculated from EDS results that (Table 2), compared with other films, T3 (TiC_{0.19}O_{1.87}) shows an abrupt decrease of C atoms content and an increase of O atoms content. Besides, the ratio of C/O trends is correlated with the variation of XRD peaks.

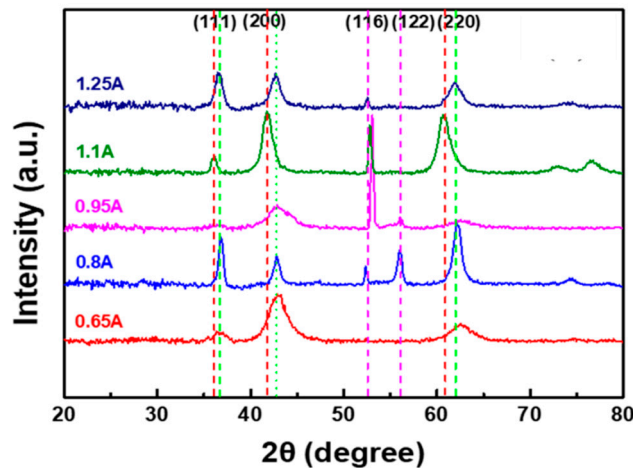


Figure 3. The X-ray diffraction (XRD) patterns: Red line, green line and purple line represent TiC, TiO_{1.04} and Ti₂O₃ peaks, respectively.

Table 2. The typical data of the TiC_xO_y films.

Films	Composition	Thickness (μm)	H ³ /E ²	Friction Coefficient	Current Density (μA/cm ²)	Ti (at.%)
T1	TiC _{0.41} O _{1.76}	0.95	0.08	0.091	1.830	32
T2	TiC _{0.27} O _{1.69}	1.58	0.14	0.085	0.033	34
T3	TiC _{0.19} O _{1.87}	1.66	0.28	0.065	0.024	33
T4	TiC _{0.29} O _{1.23}	1.97	0.25	0.071	0.340	40
T5	TiC _{0.25} O _{1.40}	2,75	0.16	0.080	257.4	38

Furthermore, cross-section SEM images and EDS element mapping of the as-deposited films were obtained, as shown in Figure 4. With the increase of the target current, the thickness of the film increases (Figure 4). Specifically, the thicknesses are 0.95, 1.58, 1.66, 1.97 and 2.75 μm, corresponding to T1, T2, T3, T4 and T5, respectively. Besides, the SEM image of T1 shows a porous and column structure (Figure 4a) and with the increase of the target current, the column structure disappears and becomes dense (T2, T3 and T4) (Figure 4b–d). However, when the target current reached to 1.25 A, the column structure presents again (Figure 4e), which might be induced by a faster growth rate that inhibits the migration and adjustment of the particles and ions involved in growth [44]. For the EDS element mapping, only T1 shows a gradient change from bottom to surface (Figure 4a) and T2 to T5 give uniform element distribution (Figure 4b–e), the gradient transition of the composition reflects that the target poisoning happened due to the low current leading to a low sputter yield gradually (Figure 4a) [45,46]. For a detailed study, the composition data are summarized in Table 2. The Ti content has almost no change until the target current of 1.1 A (T4). The sudden change of Ti content accompanies an abrupt increase of the films' thickness, which implies that the sputtering mode changed from transition to metal mode [45,46].

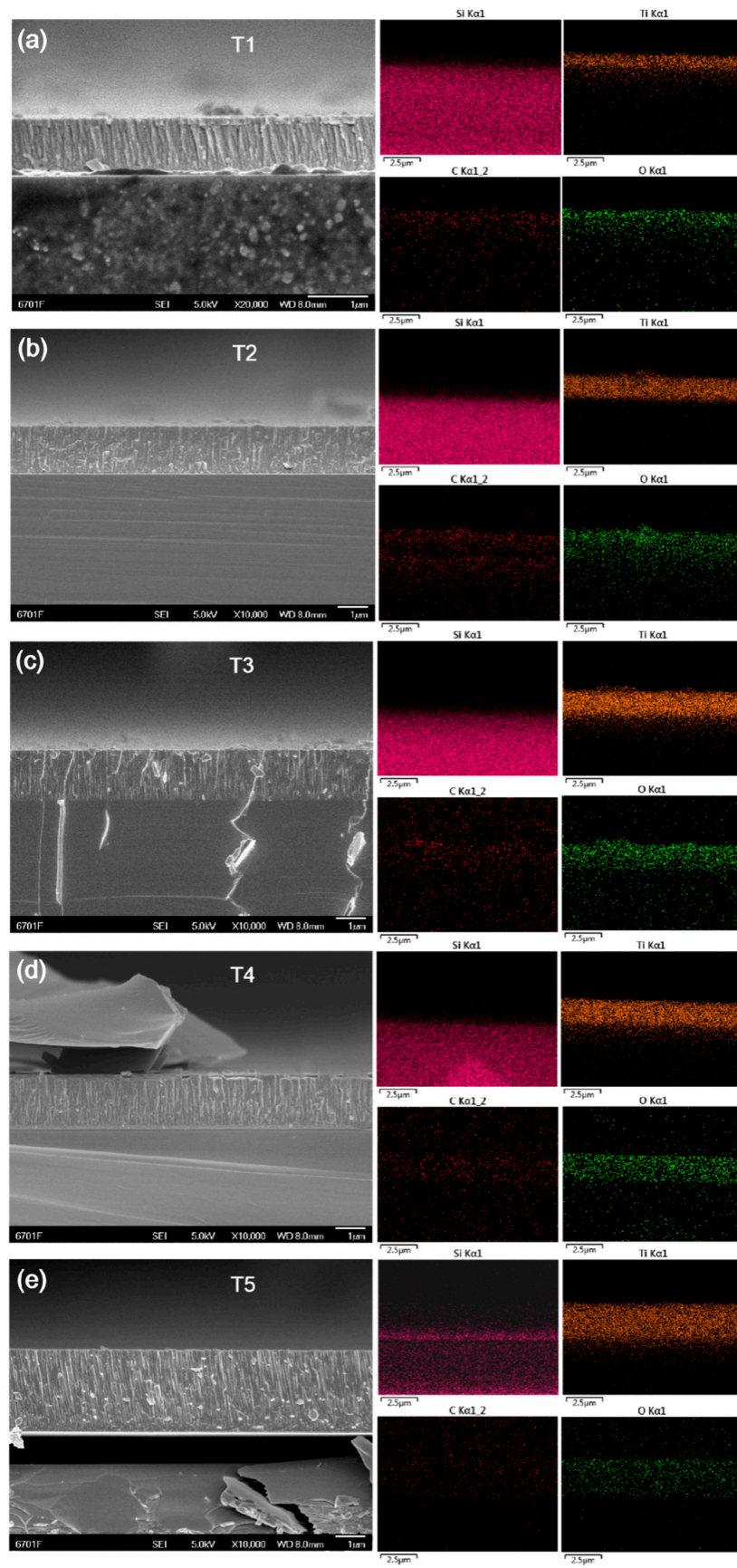


Figure 4. Cross-section scanning electron microscopy (SEM) images and EDS-map of T1 to T5 (a–e).

3.4. The Results of XPS

XPS spectra have a wide range of applications in film analysis, which can provide abundant physical and chemical information about the surface of materials. The XPS spectra of the TiC_xO_y films deposited at different target currents are presented in Figure 5. Primary peaks of C, O and Ti are all detected. The Ti2p spectra, the O1s spectra and the C1s XPS spectra, recorded from the TiC_xO_y films, are displayed in Figure 5a–c, respectively. Accordingly, TiC is represented by a C1s peak of 281.8 eV, so the C element exists in the form of titanium carbide in the TiC_xO_y films [47]. Moreover, the blue shift of C1s spectrum occurs for the TiC_xO_y film deposited at the target current of 0.95 A (T3), implying that some carbon diffused out from TiC to become isolated carbon and the Ti was oxidized further. Besides, The $\text{Ti}2p_{3/2}$ peaks of T1, T2, T4 and T5 shift to the low binding energies at about 458.5 eV (TiO_2) to further confirm the change of bonding structure variation with the adjusting of target current. The Ti2p and O1s peaks are decomposed into three peaks, according to References [48,49]. The Ti2p spectrum (Figure 5d) could be deconvoluted into three spin-orbit components under binding energies of 455.9, 456.7 and 458.5 eV and are identified with TiO, Ti_2O_3 and TiO_2 fractions in the film, respectively [48]. One can conclude that Ti_2O_3 is the dominant surface state. Furtherly, O1s spectrum (Figure 6e) can be decomposed into three bands at 528.3, 530.08 and 531.1 eV, in correlation with TiO, Ti_2O_3 and TiO_2 fractions in the film, respectively [48]. The deconvoluted result of O1s and Ti2p are consistent with each other and the collected values of $\text{Ti}_2\text{O}_3/(\text{TiO} + \text{Ti}_2\text{O}_3 + \text{TiO}_2)$ ratio of TiC_xO_y films deposited at different target current are described in Figure 6f. From the samples of T1 to T5, the percentage of Ti_2O_3 binding structure in the TiC_xO_y films is 37.1%, 42.1%, 49.1%, 40.6% and 26.7% for T2p and 39.1%, 41%, 51.8%, 32% and 26.2% for O1s, respectively. Both T2p and O1s results show a highest Ti_2O_3 binding structure the TiC_xO_y films deposited at 0.95 A (T3).

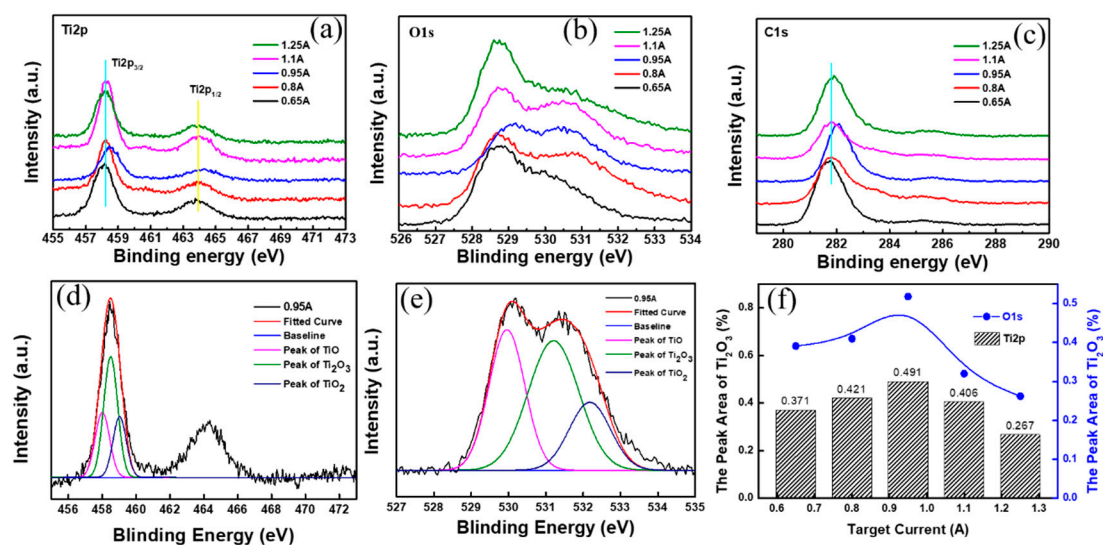


Figure 5. The X-ray photoelectron spectroscopy (XPS) spectra of (a) T2p, (b) O1s and (c) C1s for TiC_xO_y films deposited at different target current and the fitted results by a non-linear least squares procedure for TiC_xO_y films corresponding to (d) T2p, (e) O1s; (f) $\text{Ti}_2\text{O}_3/(\text{TiO} + \text{Ti}_2\text{O}_3 + \text{TiO}_2)$ ratio of TiC_xO_y films deposited at different target current.

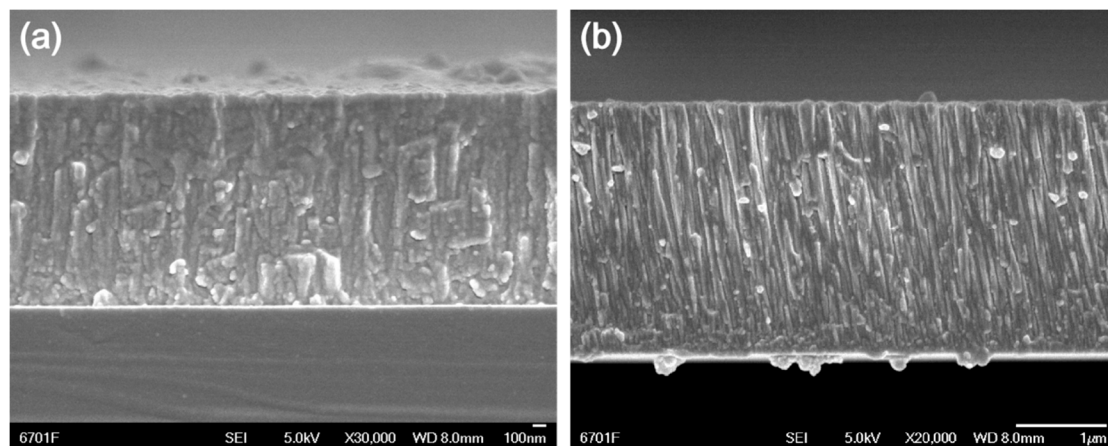


Figure 6. Microstructure comparison *via* high resolution SEM images: (a) T5 with a dense nanoparticle stacking structure and (b) T3 with a column stacking structure.

4. Discussion

One can confirm that the TiC_xO_y films are successfully grown via sputtering a Ti target in CO_2 atmosphere with Ar as a dilute gas, which proved that CO_2 is a key player in the matter of excited CO_2^+ , CO^+ , CO_3^- and so on which will be involves in the growth process reacting with Ti ions [17,27,50].

The results investigated above illustrate that the T3 sample has the highest hardness, lowest friction coefficient (Figure 1) as well as the best corrosion resistance properties (Figure 2). Some of the typical data are summarized in Table 2. It can be concluded that the composition of all samples studied in the present work are nearly unchangeable. Both the lowest C and the highest O composite are present in T3 but the $Ti/(Ti + C + O)$ ratio keeps constant until the target current increases to 1.10 A, where the Ti content increases to about 40 at.% (Table 2), which can be assigned to the sputtering modes variation from transition to metal mode [45,46] and the $O/(Ti+C+O)$ ratio fluctuation can be ascribed to the contamination of the oxygen from open atmosphere during transportation [26,27,29]. Thus, it can be confirmed that the composition has no influence on the friction and anti-corrosion properties. However, the growth rates increase with the increment of the target current (Figure 4), which can be speculated from the cross-section element mapping (Figure 4), where all the films show uniformity growth except of T1. In other words, T1 shows a gradient distribution of O and C elements which means that a heavy poisoning sputtering target occurred [45,46], so the suppressing growth rate of TiC_xO_y films happened. The target current increased from 0.80 to 1.10 A, transition zone growth mode instead of poisoning mode dominated and the growth rate increased [45,46]. At the target current of 1.25 A, a nearly metal mode presented and the growth rate increased quickly [45,46]. But the components of the TiC_xO_y film is changeable and can be assigned to high activity of CO_2 plasma [17,27,50,51].

The reason for the favorable friction properties of the sample T3 can be found from the hardness and elasticity modulus themselves. The T3 sample has the highest value of H^3/E^2 , which predicts high resistance to plastic deformation and low friction [52]. Leyland A. et al. [38] proposed that controlling the H/E ratio in frictional progress of nanocomposite coatings is extremely significant for optimal tribological behavior. The value of H/E has a critical role in determining yield pressure and crack propagation. As we known, the value of H^3/E^2 variation trends of the TiC_xO_y films are going in the opposite direction of the friction coefficients as presented in Figure 1b. Thus, combining the XRD and EDS results together (Table 2), it seems that the introduction of Ti_2O_3 phase enforces not only the hardness but also the elasticity and in turn, tunes the friction properties to a lower state. With regard to the optimal tribological behavior of coatings/films, the H^3/E^2 ratio in frictional progress is extremely significant [39]. The high value of H^3/E^2 means the improvement of the elastic recovery and toughness endow good film friction properties [38]. On the other hand, the TiO_x nano debris might be working

together to reduce friction further. As reported by Han Huang et al., the introduction of nano TiO₂ into water-based nanolubricant can decrease the friction coefficient by about 30% to some extent [53].

According to the results of EDS and XPS, no clue can be found associated with the good anti-corrosion properties of the TiC_xO_y films. Interestingly, as can be seen from Table 2, T3 has the best anti-corrosion and friction property among all the samples. It is believed that the corrosion behavior of the TiC_xO_y films depends on the dense nanoparticle stacking structure, which relates to the Ti₂O₃ phase [38].

5. Conclusions

A new method that utilizes CO₂ as precursor to deposit TiC_xO_y films by magnetron sputtering has been developed. One can confirm that CO₂ is a key player in the matter of excited CO₂⁺, CO⁺, CO₃⁻ and so on involvement in the growth process reacting with Ti ions. The obtained TiC_xO_y films hold high hardness, low friction as well as good anti-corrosion properties, which can be employed for protecting coatings for drills, engine parts, especially for those using under water lubrication state or moisture conditions that benefit from nano-TiO_x debris as liquid lubrication additives during friction. And further, the hardness, friction coefficient and anti-corrosion properties can be adjustable via target current and maybe atmosphere ratio and components and so forth. Our results could be predicting that, besides the Ti target, Si, Cr, Mo, V and Mn and so forth, could be employed as a solid source for growth MeC_xO_y films. This method does not only solidify CO₂ but also reduces CO₂ emissions via energy saving by reducing friction and resisting corrosion. Thus, we will focus on the correlation of plasma components and films' structure as well as composition, to reveal the growth mechanism and its inner factors on the tribology and corrosion properties.

Author Contributions: Conceptualization, B.Z. and K.G.; methodology, K.G.; software, Z.W. and Q.J.; validation, Z.M. and B.Z.; formal analysis, Z.M. and B.Z.; investigation, K.G.; resources, Z.W. and Q.J.; data curation, Z.W.; writing—original draft preparation, K.G. and Z.W.; writing—review & editing, K.G. and B.Z.; supervision, J.Z.; project administration, B.Z.; funding acquisition, J.Z. All authors have read and agreed to the published version of the manuscript.

Funding: This work is supported by the Youth Innovation Promotion Association CAS (No. 2017459) and National Natural Science Foundation of China (Nos. U1737213 and 51911530114).

Conflicts of Interest: The authors declare no conflict of interest.

References

1. Sanglimsuwan, K. Carbon dioxide emissions and economic growth: An econometric analysis. *Int. Res. J. Financ. Econ.* **2011**, *67*, 97–102.
2. Raupach, M.R.; Marland, G.; Ciais, P.; Le Quééré, C.; Canadell, J.G.; Klepper, G.; Field, C.B. Global and regional drivers of accelerating CO₂ emissions. *Proc. Natl. Acad. Sci. USA* **2007**, *104*, 10288–10293. [[CrossRef](#)]
3. Mardani, A.; Streimikiene, D.; Cavallaro, F.; Loganathan, N.; Khoshnoudi, M. Carbon dioxide (CO₂) emissions and economic growth: A systematic review of two decades of research from 1995 to 2017. *Sci. Total. Environ.* **2019**, *649*, 31–49. [[CrossRef](#)] [[PubMed](#)]
4. Graciani, J.; Mudiyansele, K.; Xu, F.; Baber, A.E.; Evans, J.; Senanayake, S.D.; Stacchiola, D.J.; Liu, P.; Hrbek, J.; Sanz, J.F. Highly active copper-ceria and copper-ceria-titania catalysts for methanol synthesis from CO₂. *Science* **2014**, *345*, 546–550. [[CrossRef](#)] [[PubMed](#)]
5. Chu, S.; Majumdar, A. Opportunities and challenges for a sustainable energy future. *Nature* **2012**, *488*, 294–303. [[CrossRef](#)] [[PubMed](#)]
6. Dresselhaus, M.S.; Thomas, I.L. Alternative energy technologies. *Nature* **2001**, *414*, 332–337. [[CrossRef](#)]
7. Steinlechner, C.; Junge, H. Renewable methane generation from carbon dioxide and sunlight. *Angew. Chem. Int. Ed.* **2018**, *57*, 44–45. [[CrossRef](#)]
8. Kar, S.; Sen, R.; Kothandaraman, J.; Goepfert, A.; Chowdhury, R.; Munoz, S.B.; Haiges, R.; Prakash, G.K.S. Mechanistic insights into ruthenium-pincer-catalyzed amine-assisted homogeneous hydrogenation of CO₂ to methanol. *J. Am. Chem. Soc.* **2019**, *141*, 3160–3170. [[CrossRef](#)]

9. Lee, H.; Shinn, Y.J.; Ong, S.H.; Woo, S.W.; Park, K.G.; Lee, T.J.; Moon, S.W. Fault reactivation potential of an offshore CO₂ storage site, Pohang Basin, South Korea. *J. Pet. Sci. Eng.* **2017**, *152*, 427–442. [[CrossRef](#)]
10. Kamali, A.R. Nanocatalytic conversion of CO₂ into nanodiamonds. *Carbon* **2017**, *123*, 205–215. [[CrossRef](#)]
11. Wu, Y.; Wang, T.; Wang, H.; Wang, X.; Dai, X.; Shi, F. Active catalyst construction for CO₂ recycling via catalytic synthesis of N-doped carbon on supported Cu. *Nat. Commun.* **2019**, *10*, 2599. [[CrossRef](#)] [[PubMed](#)]
12. Zhang, Z.; Wang, Z.; Cao, S.W.; Cao, S.W.; Xue, C. Au/Pt nanoparticle-decorated TiO₂ nanofibers with plasmon-enhanced photocatalytic activities for Solar-to-Fuel conversion. *J. Phys. Chem. C* **2013**, *117*, 25939–25947. [[CrossRef](#)]
13. Esrafilzadeh, D.; Zavabeti, A.; Jalili, R.; Atkin, P.; Choi, J.; Carey, B.J.; Brkljača, R.; O’Mullane, A.P.; Dickey, M.D.; Officer, D.L.; et al. Room temperature CO₂ reduction to solid carbon species on liquid metals featuring atomically thin ceria interfaces. *Nature* **2019**, *10*, 865.
14. Kang, U.; Choi, S.K.; Ham, D.J.; Ji, S.M.; Choi, W.; Han, D.S.; Abdel-Wahab, A.; Park, H. Photosynthesis of formate from CO₂ and water at 1% energy efficiency via copper iron oxide catalysis. *Energy Environ. Sci.* **2015**, *8*, 2638–2643. [[CrossRef](#)]
15. Chen, G.; Silv, T.; Georgieva, V.; Godfroid, T.; Britun, N.R.; Delplancke-ogletree, P.M. Simultaneous dissociation of CO₂ and H₂O to syngas in a surface-wave microwave discharge. *Int. J. Hydrog. Energy* **2015**, *40*, 3789–3796. [[CrossRef](#)]
16. Hyoung, S.K.; Han, S.U.; Yong, C.H.; Eun, H.C. Disintegration of carbon dioxide molecules in a microwave plasma torch. *Sci. Rep.* **2015**, *5*, 18436.
17. Wang, W.; Snoeckx, R.; Zhang, X.; Cha, M.S.; Bogaerts, A. Modeling plasma-based CO₂ and CH₄ conversion in mixtures with N₂, O₂ and H₂O: the bigger plasma chemistry. *J. Phys. Chem. C* **2018**, *122*, 8704–8723. [[CrossRef](#)]
18. Bernhardsen, I.M.; Knuutila, H.K. A review of potential amine solvents for CO₂ absorption process: Absorption capacity, cyclic capacity and pKa. *Int. J. Greenh. Gas Control* **2017**, *61*, 27–48. [[CrossRef](#)]
19. Takashi, K.; Ryo, Y.; Toshihiko, M.; Kingo, A.; Setsuo, N. Preparation of TiN films by reactive high-power pulsed sputtering Penning discharges. *Jpn. J. Appl. Phys.* **2018**, *57*, 06JE02.
20. Cao, X.; Xu, W.; He, W. A method for evaluating the impact wear behavior of multilayer TiN/Ti coating. *Coatings* **2020**, *10*, 132. [[CrossRef](#)]
21. Nguyen, D.N.; Mahesh, V.; Nguyen, T.H. Corrosion behavior of TiN, TiAlN, TiAlSiN-coated 316L stainless steel in simulated proton exchange membrane fuel cell environment. *J. Power Sources* **2014**, *268*, 240–245.
22. Krell, A.K.; Czyżniewski, A.; Gilewicz, A.; Gajowiec, G. Experimental study of the influence of deposition of multilayer CrN/CrCN PVD coating on austenitic steel on resistance to cavitation erosion. *Coatings* **2020**, *10*, 487. [[CrossRef](#)]
23. Lian, G.; Zhao, C.; Zhang, Y.; Huang, X.; Chen, C.; Jiang, J. Investigation of micro-hardness, wear resistance and defects of 316L stainless steel and TiC composite coating fabricated by laser engineered net Shaping. *Coatings* **2019**, *9*, 498. [[CrossRef](#)]
24. Huang, C.A.; Yang, S.W.; Liu, Y.W.; Lai, P.L. Effect of Cu and Ni undercoatings on the electrochemical corrosion behaviour of Cr–C-coated steel samples in 0.1 M H₂SO₄ solution with 1 g/L NaCl. *Coatings* **2019**, *9*, 531. [[CrossRef](#)]
25. Aijaz, A.; Ferreira, F.; Oliveira, J.; Kubart, T. Mechanical properties of hydrogen free diamond-like carbon thin films deposited by high power impulse magnetron sputtering with Ne. *Coatings* **2018**, *8*, 385. [[CrossRef](#)]
26. Wang, Z.; Gao, K.; Zhang, B.; Gong, Z.; Wei, X.; Zhang, J. Verification study of nanostructure evolution with heating treatment between thin and thick fullerene-like hydrogen carbon films. *Coatings* **2019**, *9*, 82. [[CrossRef](#)]
27. Qiang, L.; Gao, K.; Zhang, L.; Wang, J.; Zhang, B.; Zhang, J. Further improving the mechanical and tribological properties of low content Ti-doped DLC film by W incorporating. *Appl. Surf. Sci.* **2015**, *353*, 522–529. [[CrossRef](#)]
28. Gao, K.; Wang, Y.; Wei, X.; Qiang, L.; Zhang, B.; Zhang, J. Hydrogenated amorphous carbon films with different nanostructure: a comparative study. *Chem. Phys. Lett.* **2019**, *715*, 330–334. [[CrossRef](#)]
29. Zhao, Q.; Mou, Z.; Zhang, B.; Zhang, X.; Wang, Z.; Wang, K.; Gao, K.; Jia, Q. Revealing the corrosion resistance of amorphous carbon films under heat shock via annealing. *Diam. Relat. Mater.* **2020**, *102*, 107692. [[CrossRef](#)]

30. Wang, Z.; Gong, Z.; Zhang, B.; Wang, Y.; Gao, K.; Zhang, J.; Liu, G. Heating induced nanostructure and superlubricity evolution of fullerene-like hydrogenated carbon films. *Solid State Sci.* **2019**, *90*, 29–33. [[CrossRef](#)]
31. Qiang, L.; Zhang, B.; Zhou, Y.; Zhang, J. Improving the internal stress and wear resistance of DLC film by low content Ti doping. *Solid State Sci.* **2013**, *20*, 17–22. [[CrossRef](#)]
32. Fernandes, A.C.; Carvalho, P.; Vaz, F.; Lanceros-Méndez, S.; Machado, A.V.; Parreir, N.M.G.; Pierson, J.F.; Martin, N. Property change in multifunctional TiC_xO_y thin films: Effect of the O/Ti ratio. *Thin Solid Films* **2006**, *515*, 866–871. [[CrossRef](#)]
33. Fernandes, A.C.; Vaz, F.; Rebouta, L.; Pinto, A.; Alves, E.; Parreir, N.M.G.; Goudeau, Ph.; Bourhis, E.L.; Rivière, J.P. Influence of the O/C ratio in the behaviour of TiC_xO_y thin films. *Surf. Coat. Technol.* **2007**, *201*, 5587–5591. [[CrossRef](#)]
34. Carvalho, P.; Vaz, F.; Rebouta, L.; Cunha, L.; Tavares, C.J.; Moura, C.; Alves, E.; Cavaleiro, A.; Goudeau, P.; Bourhis, E.L.; et al. Structural, electrical, optical and mechanical characterization of decorative ZrO_xN_y thin films. *J. Appl. Phys.* **2005**, *98*, 023715. [[CrossRef](#)]
35. Mathew, M.T.; Ariza, E.; Rocha, L.A.; Fernandes, A.C.; Vaz, F. TiC_xO_y thin films for decorative applications: Tribocorrosion mechanisms and synergism. *Tribol. Int.* **2008**, *41*, 603–615. [[CrossRef](#)]
36. Mathew, M.T.; Ariza, E.; Rocha, L.A.; Fernandes, A.C.; Vaz, F. Tribocorrosion behaviour of TiC_xO_y thin films in bio-fluids. *Electrochim. Acta* **2010**, *56*, 929–937. [[CrossRef](#)]
37. Garcia-Cosio, G.; Calixto-Rodriguez, M.; Martinez, H. Low-pressure plasma discharge of $Ar/N_2/CO_2$ ternary mixture. Topic number B6200954. In Proceedings of the 29th International Conference on Phenomena in Ionized Gases (ICPIG 2009), Cancun, Mexico, 12–17 July 2009.
38. Leyland, A.; Matthews, A. On the significance of the H/E ratio in wear control: A nanocomposite coating approach to optimised tribological behaviour. *Wear* **2000**, *246*, 1–11. [[CrossRef](#)]
39. Galvan, D.; Pei, Y.T.; Hosson, J.T.M.D. Deformation and failure mechanism of nano-composite coatings under nano-indentation. *Surf. Coat. Technol.* **2006**, *200*, 6718–6726. [[CrossRef](#)]
40. Devia, D.M.; Restrepo, J.; Ruden, A.; González, J.M.; Sequeda, F.; Arango, P.J. The tribological characteristics of TiN, TiC, TiC/TiN films prepared by reactive pulsed arc evaporation technique. In Proceedings of the 52nd Annual Technical Conference, Santa Clara, CA, USA, 9–14 May 2009.
41. Chen, Y.; Mao, J. Sol-gel preparation and characterization of black titanium oxides Ti_2O_3 and Ti_3O_5 . *J. Mater. Sci.: Mater. Electron* **2014**, *25*, 1284–1288. [[CrossRef](#)]
42. Wu, X.W.; Wu, D.J.; Liu, X.J. Silver-doping induced lattice distortion in TiO_2 nanoparticles. *Chin. Phys. Lett.* **2009**, *7*, 077809.
43. Afifi, M.A.; Abdel-Aziz, M.M.; Yahia, I.S.; Fadel, M.; Wahab, L.A. Transport properties of polycrystalline TiO_2 and Ti_2O_3 as semiconducting oxides. *J. Alloy. Compd.* **2008**, *455*, 92–97. [[CrossRef](#)]
44. Ma, T.B.; Hu, Y.Z.; Wang, H. Role of atomic transverse migration in growth of diamond-like carbon films. *Chin. Phys.* **2007**, *16*, 2798–2802.
45. Haase, F.; Kersten, H.; Lundin, D. Plasma characterization in reactive sputtering processes of Ti in Ar/O_2 mixtures operated in metal, transition and poisoned modes: a comparison between direct current and high-power impulse magnetron discharges. *Eur. Phys. J. D* **2017**, *71*, 245. [[CrossRef](#)]
46. Akazawa, H. Sputtering characteristics, crystal structures and transparent conductive properties of TiO_xN_y films deposited on $\alpha-Al_2O_3(0001)$ and glass substrates. *Appl. Surf. Sci.* **2012**, *263*, 307–313. [[CrossRef](#)]
47. Zhang, L.; Koka, R.V. A study on the oxidation and carbon diffusion of TiC in alumina–titanium carbide ceramics using XPS and Raman spectroscopy. *Mater. Chem. Phys.* **1998**, *57*, 23–32. [[CrossRef](#)]
48. Lewin, E.; Persson, P.O.Å.; Lattemann, M.; Stüber, M.; Gorgoi, M.; Sandell, A.; Ziebert, C.; Schäfers, F.; Braun, W.; Halbritter, J.; et al. On the origin of a third spectral component of C1s XPS-spectra for nc-TiC/a-C nanocomposite thin films. *Surf. Coat. Technol.* **2008**, *202*, 3563–3570. [[CrossRef](#)]
49. Kumar, P.M.; Badrinarayanan, S.; Sastry, M. Nanocrystalline TiO_2 studied by optical, FTIR and X-ray photoelectron spectroscopy: correlation to presence of surface states. *Thin Solid Films* **2000**, *358*, 122–130. [[CrossRef](#)]
50. Zalar, A.; Kovac, J.; Pracek, B.; Panjan, P.; Ceh, M. Ion sputtering rates of W-, Ti- and Cr-carbides studied at different Ar^+ ion incidence angles. *Appl. Surf. Sci.* **2008**, *254*, 6611–6618. [[CrossRef](#)]

51. Aleksandrov, N.L.; Kindysheva, S.V.; Kirpichnikov, A.A.; Kosarev, I.N.; Starikovskii, A.Y. Plasma decay in N_2 , CO_2 and H_2O excited by high-voltage nanosecond discharge. *J. Phys. D: Appl. Phys.* **2007**, *40*, 4493. [[CrossRef](#)]
52. Nikolett, O.; Zsolt, F.; Attila, S.; János, S.; Tamás, C.; Katalin, B. Ceramic TiC/a:C protective nanocomposite coatings: Structure and composition versus mechanical properties and tribology. *Ceram. Int.* **2016**, *42*, 12215–12220.
53. Wu, H.; Jia, F.; Zhao, J.; Huang, S.; Wang, L.; Jiao, S.; Huang, H.; Jiang, Z. Effect of water-based nanolubricant containing nano- TiO_2 on friction and wear behaviour of chrome steel at ambient and elevated temperatures. *Wear* **2019**, *426–427*, 792–804. [[CrossRef](#)]



© 2020 by the authors. Licensee MDPI, Basel, Switzerland. This article is an open access article distributed under the terms and conditions of the Creative Commons Attribution (CC BY) license (<http://creativecommons.org/licenses/by/4.0/>).